Probing the Innermost Regions of AGN Jets and Their Magnetic Fields with RadioAstron. III. Blazar S5 0716+71 at Microarcsecond Resolution

E. V. Kravchenko[1,2], J. L. Gómez[3], Y. Y. Kovalev[2,4,5], A. P. Lobanov[5,6], T. Savolainen[5,7,8], G. Bruni[9], A. Fuentes[3], J. M. Anderson[10], S. G. Jorstad[11,12], A. P. Marscher[11], M. Tornikoski[8], A. Lähteenmäki[7,8], and M. M. Lisakov[2,5]

[1] INAF Istituto di Radioastronomia, Via P. Gobetti, 101, Bologna, I-40129, Italy; e.kravchenko@ira.inaf.it
[2] Astro Space Center, Lebedev Physical Institute, Russian Academy of Sciences, Profsoyuznaya st., 84/32, Moscow, 117997, Russia
[3] Instituto de Astrofísica de Andalucía, CSIC, Glorieta de la Astronomía s/n, Granada, E-18008, Spain
[4] Moscow Institute of Physics and Technology, Institutsky per. 9, Moscow region, Dolgoprudny, 141700, Russia
[5] Max-Planck-Institut für Radioastronomie, Auf dem Hügel 69, Bonn, D-53121, Germany
[6] Institut für Experimentalphysik, Universität Hamburg, Luruper Chaussee, 149, D-22761 Hamburg, Germany
[7] Aalto University Department of Electronic and Nanoengineering, PL15500, FI-00076 Aalto, Finland
[8] Aalto University Metsähovi Radio Observatory, Metsähovintie 114, FI-02540 Kylmälä, Finland
[9] INAF-Istituto di Astrofisica e Planetologia Spaziali, via Fosso del Cavaliere, 100, I-00133 Rome, Italy
[10] Deutsches GeoForschungsZentrum GFZ, Telegrafenberg, D-14473 Potsdam, Germany
[11] Institute for Astrophysical Research, Boston University, 725 Commonwealth Avenue, Boston, MA 02215, USA
[12] Astronomical Institute, St. Petersburg University, Universitetskij Pr. 28, Petrodvorets, 198504 St. Petersburg, Russia
Received 2019 March 5; revised 2020 February 21; accepted 2020 March 4; published 2020 April 16

Abstract

We present RadioAstron Space VLBI imaging observations of the BL Lac object S5 0716+71 made on 2015 January 3–4 at a frequency of 22 GHz (wavelength $\lambda = 1.3$ cm). The observations were made in the framework of the AGN Polarization Key Science Program. The source was detected on projected space–ground baselines up to 70,833 km (5.6 Earth diameters) for both parallel-hand and cross-hand interferometric visibilities. We have used these detections to obtain a full-polarimetric image of the blazar at an unprecedented angular resolution of 24 μas, the highest for this source to date. This enabled us to estimate the size of the radio core to be $<12 \times 5 \ \mu$as and to reveal a complex structure and a significant curvature of the blazar jet in the inner 100 μas, which is an indication that the jet viewing angle lies inside the opening angle of the jet conical outflow. Fairly highly (15%) linearly polarized emission is detected in a jet region 19 μas in size, located 58 μas downstream from the core. The highest brightness temperature in the source frame is estimated to be $>2.2 \times 10^{13}$ K for the blazar core. This implies that the inverse-Compton limit must be violated in the rest frame of the source, even for the largest Doppler factor $\delta \sim 25$ reported for 0716+714.

1. Introduction

S5 0716+71 (hereafter 0716+714) is one of the most active BL Lac objects and the subject of numerous studies carried out since its discovery in 1979 by Kuehr et al. (1981). It is extremely variable throughout the whole electromagnetic spectrum, with timescales that range from hours to months, including intra-day variability (IDV; e.g., Ostorero et al. 2006; Liao et al. 2014). The duty cycle of the source is about 80%–90% (e.g., Wagner & Witzel 1995; Hu et al. 2014), which implies that it is active almost all the time. It is considered one of the best candidates for having an intrinsic origin of the observed IDV (e.g., Quirrenbach et al. 1989; Gupta et al. 2012), rather than being produced by scintillation in the ionized interstellar medium (ISS, Rickett et al. 1984). There is a large amount of evidence supporting this: the observed increase in variability amplitude with frequency (Fuhrmann et al. 2008); the correlation between optical brightness and radio spectral index, as well as simultaneous change in variability timescale (Wagner et al. 1990, 1996); the rapid variability at millimeter wavelengths (Ostorero et al. 2006); the quasi-periodic intra-hour oscillations at the optical band (Rani et al. 2010); and the highly polarized optical microflares (Bhatta et al. 2015). However, the observed annual modulation of the variability

pattern (Liu et al. 2012) implies that some of the variability observed in 0716+714 is produced by interstellar scintillation, at least at 6 and 11 cm (see also Gupta et al. 2012).

Very long baseline interferometry (VLBI) observations of 0716+714 show that the radio continuum emission is dominated by a bright core, with occasional ejection of superluminal components with apparent velocities as high as 25c (Bach et al. 2005, 2006; Rastorgueva et al. 2009; Jorstad et al. 2017; Lister et al. 2019). A joint analysis of the jet kinematic properties and the variability of radio emission in 0716+714 yields estimates of Doppler factor $4 \leqslant \delta \leqslant 25$, with bulk jet Lorentz factor $10 \leqslant \Gamma \leqslant 25$ at viewing angle $\theta \leqslant 5°$ (Bach et al. 2005; Hovatta et al. 2009; Jorstad et al. 2017).

First space VLBI (SVLBI) observations of 0716+714, performed with the VLBI Space Observatory Program (VSOP), were reported by Bach et al. (2006), revealing that the IDV observed in 0716+714 both in the total and polarized emission may originate within the unresolved $<100 \ \mu$as VLBI core. From the variability timescales assuming the internal nature of the IDV they estimated a source size of a few μas, well below the angular resolution provided by VSOP.

Launched in 2011 and observing until 2019 January, the RadioAstron space VLBI mission (Kardashev et al. 2013) featured a 10 m antenna on board the Spektr-R satellite.

Revolving around the Earth on an elliptical orbit reaching 360,000 km, it enabled probes of celestial objects with a maximum angular resolution of 7 μas (Kardashev et al. 2017). The space radio telescope (SRT) operated in four wavelength bands: P (0.33 GHz, $\lambda = 92$ cm), L (1.6 GHz, $\lambda = 18$ cm), C (4.8 GHz, $\lambda = 6.2$ cm), and K (18–26 GHz, $\lambda = 1.2$–1.6 cm). Polarized emission could be studied with RadioAstron in the P, L, and K bands in dual circular polarization mode, with the left circularly polarized (LCP) and right circularly polarized (RCP) channels for recording data.

Blazar 0716+714 was the first AGN imaged with Radio-Astron. Observations were made on 2012 March 14–15 at 4.8 GHz during the Early Science Program period (Kardashev et al. 2013). One of the RadioAstron Key Science Program (KSP) continued these experiments, particularly focusing on the polarimetry of the most active and highly polarized AGNs in the sky. The Polarization KSP has collected data throughout the whole RadioAstron science program. The first test polarimetric observations were performed on 2013 March 9–10 at 18 cm, targeting the quasar TXS 0642+449 (Lobanov et al. 2015). The total and linearly polarized emission was detected at baselines up to 75,560 km ($\sim$6 Earth diameters, ED), resulting in an angular resolution of 0.8 mas. It was shown that instrumental polarization (leakage between the two polarization channels) of the space antenna is smaller than 9%, demonstrating the RadioAstron polarization capabilities for high-fidelity polarization imaging (see also Pashchenko et al. 2015). The first polarimetric experiment at 1.3 cm took place on 2013 November 10 (Gómez et al. 2016), when BL Lacertae was detected on the projected baselines up to $\sim$8 ED, delivering the image with the highest angular resolution achieved to date, 21 μas. The instrumental polarization of the SRT was found to be less than 9%, demonstrating the possibility of carrying out polarization measurements with RadioAstron at its highest observing frequency. The combination of RadioAstron 22 GHz and quasi-simultaneous ground-based 15 and 43 GHz images resulted in detecting a gradient in rotation measure (RM) and intrinsic polarization vector as a function of position angle with respect to the core of BL Lacertae, suggesting that the blazar jet is threaded by a helical magnetic field. The intrinsic de-boosted brightness temperature in the unresolved core of the source was estimated to be $>3 \times 10^{12}$ K, in excess of theoretical limits (Kellermann & Pauliny-Toth 1969; Readhead 1994).

Recently, Bruni et al. (2017) presented the results of the SVLBI imaging experiment of the quasar 3C273 on 2014 November 18–19 at 22 GHz. The observations probed the source during a particularly low activity state, yielding a brightness temperature at the level of 5×10^9 K. Kovalev et al. (2016) reported an almost two orders of magnitude higher value of 1.4×10^{13} K, based on the RadioAstron observations of the quasar on 2013 February 2 at the same frequency. Bruni et al. (2017) concluded that the detected extreme brightness temperatures in the quasar seen by Kovalev et al. (2016) one year before their study represent a short-lived phenomenon caused by a temporary departure from the equipartition between the radiating particles and magnetic field energy density. This implies that the source state plays a principal role in the characterization of the observable physical quantities.

This paper continues a series of studies of AGN jets within the RadioAstron Polarization KSP: we present here our observations of 0716+714 probing the jet structure at the finest angular resolution possible to investigate the origin of the

Table 1
Radio Telescopes Participating in RadioAstron Observations of 0716+714

Telescope	Code	D (m)	SEFD (Jy)	BW (MHz)	B_{max} (ED)
Spektr-R (Space)	RA	10	4670[a], 3680[b]	32	4.96
Brewster (USA)	BR	25	640	64	4.81
Effelsberg (Germany)	EF	100	90	128	4.68
Ford Davis (USA)	FD	25	640	64	4.93
Green Bank (USA)	GB	100[c]	30	64	4.96
Hancock (USA)	HN	25	640	64	0.40
Los Alamos (USA)	LA	25	640	64	4.91
Noto (Italy)	NT	32	800	128	0.66
Owens Valley (USA)	OV	25	640	64	4.81
Pie Town (USA)	PT	25	640	64	4.91
Shanghai (China)	SH	65	1700	128	0.72
Torun (Poland)	TR	32	500	128	0.59

Note. D: antenna diameter ([c]: equivalent diameter); SEFD: system equivalent flux density at 22 GHz ([a] for LCP, [b] for RCP); BW: observing bandwidth per each circular polarization; Bmax: largest projected baseline in detections, in units of Earth diameter.

IDV and reconstruct the magnetic field in the vicinity of the central black hole.

The 0716+714 has no identified spectroscopic redshift because of a featureless optical continuum and bright nucleus in the optical. Most recent attempts to measure the blazar redshift have constrained it within a range of $0.2315 < z < 0.3407$ (Danforth et al. 2013), based on the detection of Lyα systems in the far ultraviolet spectrum of the source. This is consistent with the photometric detection of the blazar's host galaxy at $z = 0.31 \pm 0.08$ (Nilsson et al. 2008). Recently MAGIC Collaboration et al. (2018) used simultaneous spectra from MAGIC and Fermi-LAT at energies above 0.1 GeV and estimated the blazar redshift to be $z = 0.31 \pm 0.05$. We adopt this value throughout the paper.

We assume the flat ΛCDM cosmology with a matter density $\Omega_m = 0.3$, cosmological constant $\Omega_\Lambda = 0.7$ and Hubble constant $H_0 = 70$ km s^{-1} Mpc^{-1}, (Bennett et al. 2014; Planck Collaboration et al. 2016), which corresponds to the luminosity distance $D_L = 1.6$ Gpc and gives a scale of 4.56 pc per 1 mas at redshift 0.31.

2. Observations and Data Reduction

2.1. RadioAstron Imaging Experiment

The imaging experiment on 0716+714 was performed in 2015 January 3–4 at 22.2 GHz during a 12 hr space VLBI session (RadioAstron project code raks11aa, global VLBI project code GL041A). Out of 20 scheduled ground stations, 8 were lost due to different technical problems: Metsähovi (Finland), Robledo (Spain), Jodrell Bank (UK), Sardinia (Italy), Yebes (Spain), North Liberty (USA), Kitt Peak (USA), St. Croix (USA), and Maunakea (USA). Twelve ground antennas delivered data that could be used for the correlation. They are listed in Table 1, along with their basic parameters.

The data were recorded in two circular polarizations (right and left, RCP and LCP) starting from the frequency of 22220 MHz in a bandwidth of 32, 64, and 128 MHz per polarization, depending on the radio antenna (See Table 1 for details). Each bandwidth was split into 2, 4, and 16 MHz intermediate frequency (IF) channels, respectively. Two

calibrators, 4C+39.25 and 0836+710, were observed only by the ground array during the gaps required to cool down the motor drive of the onboard high-gain antenna of the Spektr-R satellite. These gaps were also used to schedule several scans at 15 and 43 GHz with the VLBA stations in order to provide a quasi-simultaneous multi-frequency coverage of our target. Unfortunately, due to the loss of the data at four of the VLBA antennas, the resulting 15 and 43 GHz data sets were insufficient to obtain reliable images at these frequencies.

The VLBI experiment was correlated using the upgraded *ra* version of the DiFX correlator developed at the Max-Planck-Institüt für Radioastronomie (MPIfR) in Bonn (Bruni et al. 2016). At the correlation stage, a rough fringe search on ground-to-space baselines was performed starting from the scans nearest to the spacecraft perigee, corresponding to a projected baseline of about 4 ED for this experiment. A significant interferometric signal was found up to about 5 ED. For the remaining scan solutions, delay and delay-rate were extrapolated from the previous ones in order to optimize the centering of the correlation window.

Data reduction and hybrid imaging were performed in AIPS (Greisen 2003) and Difmap (Shepherd et al. 1994; Shepherd 1997). Following the procedure for calibrating RadioAstron data described in Gómez et al. (2016), we first performed a fring-fitting of the ground array, and then coherently phased it to search for the fring solutions of the space antenna. We were able to find significant fringes between ground antennas and the space telescope at the maximum projected baseline of 5.25 Gλ, or 5.56 ED (70 833 km). No fringes to the SRT were found for two scans at about 6 ED despite integrating the signal from the two polarizations and IFs. We considered the a priori visibility amplitude accuracy at the level of 13%. The delay difference between the two polarization was corrected using the task RLDLY in AIPS. The instrumental polarization (or leakage) was derived with the task LPCAL in AIPS, using our target 0716+714, since it is the only source observed with the Spektr-R radio antenna; additionally, it contains the best parallactic-angle coverage among all the observed sources. Calibration of the absolute EVPA orientation was obtained through comparison with the quasi-simultaneous observations of our target and calibrators obtained with the Effelsberg single dish at 2.8 cm and 6 cm (epoch 2015 January 1), VLBA-MOJAVE at 2 cm (2015 January 18), and VLBA-BU at 7 mm (2014 December 29 and 2015 February 14). We estimate our absolute EVPA values to be accurate within 6°.

2.2. Single-dish Monitoring at 37 GHz

Metsähovi Radio Observatory has a dedicated program to monitor a sample of extragalactic radio sources, including bright AGNs, that has been running since 1980 using 13.7 m diameter antenna (Teraesranta et al. 1998). The program comprises regular observations of the total flux density mainly at 22 and 37 GHz. We made use of these 37 GHz data in our analysis.

2.3. 43 GHz VLBA Observations

Our study makes use of 43 GHz VLBA data from the VLBA-BU-BLAZAR monitoring program.[13] A total of 50 epochs of 0716+714 were used, covering the period from 2012 January 27 until 2017 April 16, with an approximately monthly

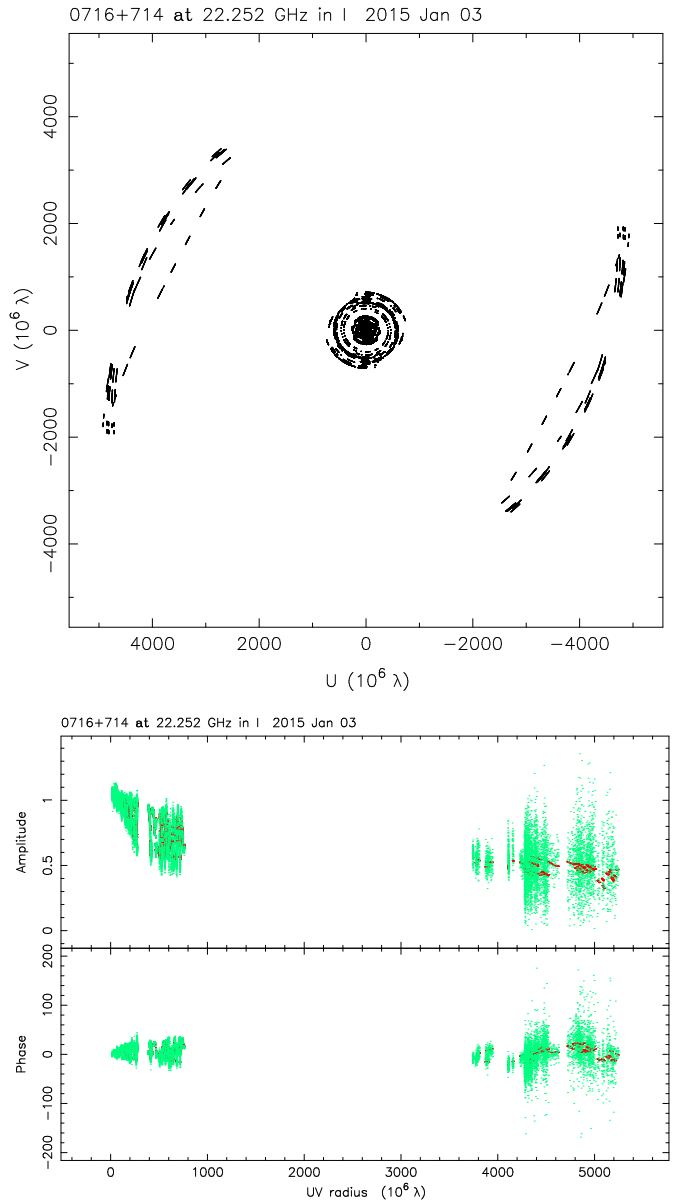---
[13] http://www.bu.edu/blazars/VLBAproject.html

Figure 1. (Top) Coverage of the *uv*-space Fourier domain for RadioAstron detections of 0716+714 on 2015 January 3–4 at 22 GHz. (Bottom) Self-calibrated visibility amplitudes (Jy) and phases (degrees) vs. *uv*-distance for the same experiment. The CLEAN model obtained from hybrid mapping is overlaid in red. Space–ground baselines start at ∼3500 Mλ (1 ED ∼ 940 Mλ).

cadence. Further details about the VLBA-BU-BLAZAR program and the calibration of these data can be found in Jorstad et al. (2017).

3. Results

3.1. 22 GHz SVLBI Image and Jet Structure

Figure 1 shows the coverage in the visibility domain, the so-called *uv*-coverage, of the fringe-fitted solutions for our RadioAstron observations of 0716+714 in 2015 January 3–4 at 22 GHz. The resulting polarization space VLBI images of the blazar are shown in Figure 2 using three different weightings: natural, uniform, and "super" uniform, when the gridding weights of the visibilities for the longest baseline and particularly for the RadioAstron are not scaled by visibility
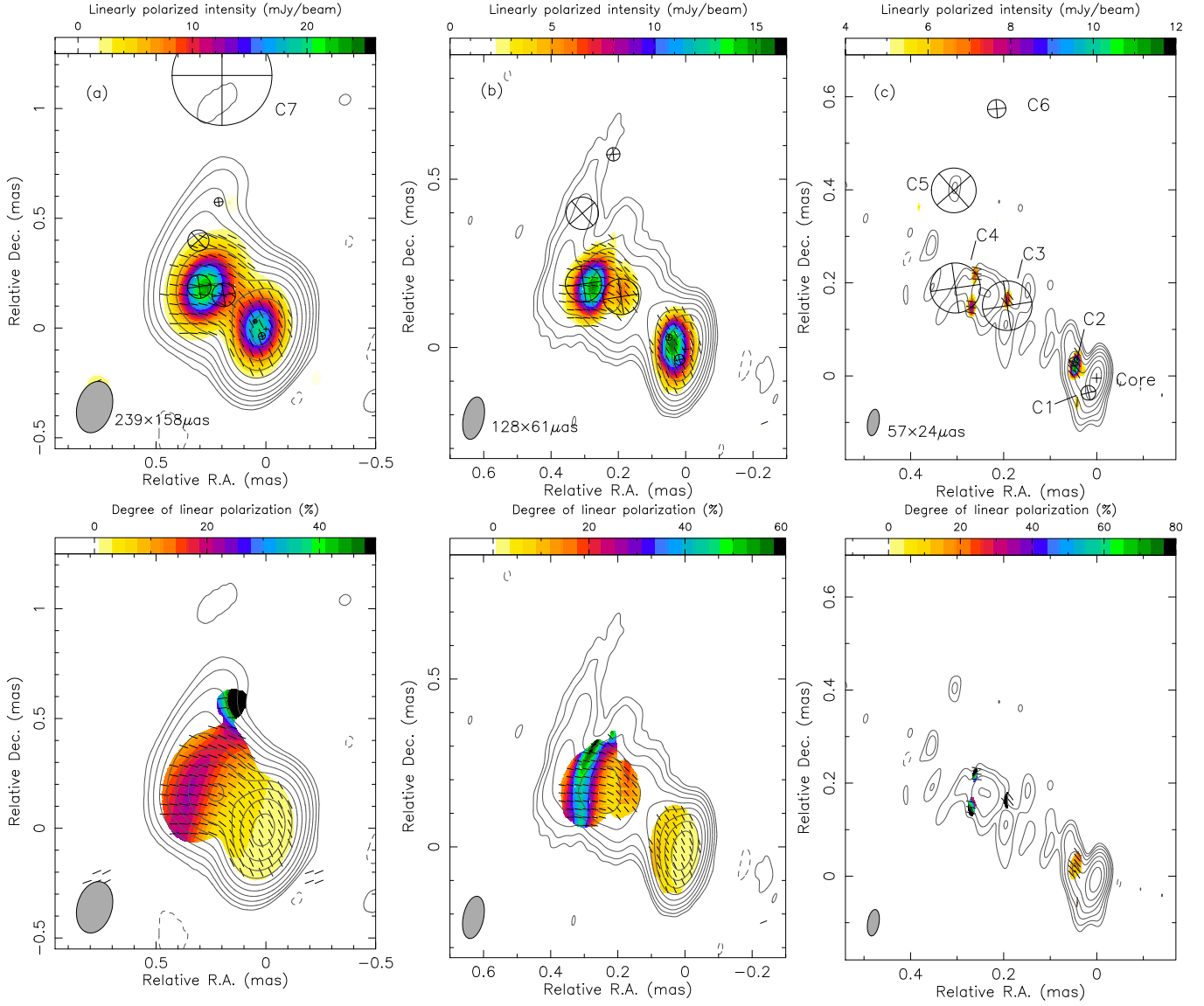
Figure 2. (Upper row) RadioAstron polarimetric and total intensity SVLBI image of 0716+714 obtained on 2015 January 3–4 at 22 GHz with (a) natural, (b) uniform, and (c) super-uniform weighting. The total intensity contours are the following: (a) −0.8, 0.8, 1.7, 3.4, 6.8, 13.5, 27.0, 54.1, 108.1, 216.3, 432.6 mJy beam^{-1}; (b) −1.4, 1.4, 2.8, 5.6, 11.2, 22.3, 44.6, 89.2, 178.5, 356.9 mJy beam^{-1}; and (c) −4.5, 4.5, 8.9, 17.8, 35.7, 71.3, 142.6, 285.3 beam^{-1}. Linearly polarized intensity is shown by color, and the value of $\sigma_{\rm rms}$ corresponds to (a) 0.26, (b) 0.30 and (c) 1.51 mJy beam^{-1}. The synthesized beam is given at position angles of (a) −15°9, (b) −11°8, and (c) −9°3, and is displayed by a shaded ellipse in the left bottom corner. Circles and crosses indicate the positions and the sizes (FWHM) of Gaussian components, which were model-fitted to the visibility data in the uv-plane. (Bottom row) Same as above, but for the degree of linear polarization.

amplitude errors and thus increase from natural to super-uniform weightings. This therefore yields the higher angular resolution, achieving about 24 μas, but lower image sensitivity for the super uniformly weighted image. Nonetheless, Martí-Vidal et al. (2012) showed that the over-resolution power of an interferometer (the minimum possible size of a source whose structure can be detected) is a function of its sensitivity, implying that an interferometer is capable of resolving structures below the diffraction limit $\lambda/B_{\rm max}$ (known as super-resolution). Considering the emission in the inner 100 μas of the 0716+714 jet, we estimate the signal-to-noise ratio (S/N) at the level of ∼30–90. Following Martí-Vidal et al. (2012) and considering the uniformly weighted beam size $\theta_{\rm beam}$ enables us to probe the details of the jet down to ∼$\theta_{\rm beam}/{\rm S/N}^{0.5}$ ∼ few μas, justifying usage of the super-resolution.

To build a RadioAstron image, we made use of closure quantities, as they are helpful for constraining the overall source structure (Rogers et al. 1974; Readhead et al. 1988). Particularly, the closure phase represents a directed sum of visibility phases around an interferometric triangle, which cancels out the station-based phase errors on each individual visibility (Jennison 1958). We computed the χ^2-statistics for the closure phase, $\chi^2_{\rm CP}$, and closure amplitude, $\chi^2_{\rm logCA}$, to quantify the agreement between the reconstructed image and the data following Event Horizon Telescope Collaboration et al. (2019a). We have compared these quantities for the models with and without the extension of the core in the southeast direction. It turned out that the model without the extension has χ^2 values higher by a coefficient of 2.8 and 2.4 than the model with the extension for the closure phases and amplitudes, respectively. Among a few alternatives, the
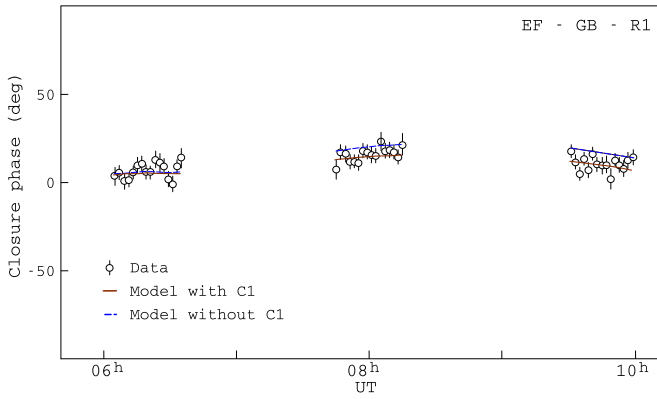
Figure 3. Selected, non-zero closure phases of 0716+714 as a function of time formed on the triangle RadioAstron–Effelsberg–Green Bank, along with the fitted models with and without component C1 discussed in Section 3.1. The χ^2 value evaluating the model fit with component C1 is 2.8 times lower than that for the model without component C1.

presented 0716+714 image provides the best overall fit to the data, especially to the non-zero closure phases between RadioAstron, and the most sensitive ground radio antennas, namely Green Bank and Effelsberg (See Figure 3). We examined an affect of amplitude calibration of the space antenna on these results. Variation of the amplitude correction within 10% yields no significant changes, supporting the robustness of the obtained 0716+714 image and extension of the core in particular. Nevertheless, future space and millimeter VLBI observations at similarly high angular resolution as those presented here, now possible thanks to the Event Horizon Telescope (Event Horizon Telescope Collaboration et al. 2019b), will be required to test the reliability of the obtained 0716+714 model.

The observed brightness distribution in the jet was represented by a number of circular two-dimensional Gaussian components, which were fitted to the visibility data, using task *modelfit* in Difmap. These model-fitted Gaussian components are shown in Figure 2 and their parameters are listed in Table 2. The standard deviations for the fitted flux density, position, and size were calculated using the *showmodel* routine in Difmap.

The RadioAstron image in the right panel of Figure 2 shows a complex, bent structure in the central 0.1 mas core region consisting of an unresolved core and nearby components C1 and C2, located at 40.5 and 58.0 μas from the core, respectively. The jet initially extends toward the southeast, where component C1 is located at a position angle of 153°7, followed by a sharp bending of about 95° toward the northeast, maintaining that direction for about 1 mas until another sharp bend toward the northwest is observed. For the unresolved VLBI core we have estimated an upper limit of its size following Lobanov (2005), yielding $\theta_{core} < 12 \times 5\,\mu$as.

The VLBA image of 0716+714 made at 1.4 GHz by the MOJAVE program[14] shows that the jet changes its PA from about 26° to about −50° at a distance of about 70 mas from the core. The progressively larger-scale VLA image of Gabuzda et al. (2000) obtained at 5 GHz shows that the 0716+714 jet extends more than 4 arcsec downstream, at the jet PA of ∼−60°. Considering the direction of both the component C1

and the arcsec-scale jet relative to the core, it yields about 210° offset between their orientations in projection on the sky plane.

As 0716+714 is oriented close to the line of sight, intrinsic variations of the jet PA should be significantly amplified in projection of the sky. Assuming a jet viewing angle of $\theta \leqslant 5°$, the apparent bend then corresponds to an actual change of $210° \times \sin\theta \lesssim 10°$. See, e.g., Savolainen et al. (2006) for a discussion of possible mechanisms capable of producing curved structures in AGN jets.

A stacked-epoch analysis of VLBA images shows that the intrinsic opening angle of 0716+714 jet is $1°6 \pm 0°2$ (Pushkarev et al. 2017). Thus, we can observe the inner jet of the source at a viewing angle smaller than its opening angle, i.e., directly inside the outflow (Lister et al. 2013). Therefore, the inner jet may appear bent as individual emerging features are ejected at different PAs (e.g., Rani et al. 2015) and fill the entire width of the jet.

3.2. Linear Polarization and RM

The naturally weighted and uniformly weighted RadioAstron images in Figure 2 show that the linearly polarized emission of 0716+714 is dominated by two main features: one associated with the core area and a second one located in the jet, near component C4. The super-uniformly weighted image in the right panel of Figure 2 shows weakly polarized structures located near the component C2 and farther downstream in the jet.

As was stated above, the quality of the 15 and 43 GHz VLBA data taken during the RadioAstron cooling gaps was not good enough for carrying out Faraday RM analysis, since four antennas of the array were lost during our observations. Moreover, no MOJAVE observations of 0716+714 were performed close to our epoch. This limited our analysis to two frequencies: our 22 GHz data and the BU-BLAZAR 43 GHz data at a close epoch (2014 December 29, see Figure 4). A Faraday rotation analysis based solely on two-frequency data can be performed under the assumption of negligible internal Faraday rotation, in which case we could expect a linear dependence of the polarization vector with the square of the observing frequency. To account for the $n\pi$ ambiguity in the polarization vector we further assume the smallest Faraday rotation. We also note that higher values of n would result in large RM values, and therefore significant bandwidth depolarization, which are not observed. Finally, the RM images of Figure 4 are also performed under the assumption that the polarization structure is not changed in the time lapse between our two-frequency observations, and that any differences between polarization angles at the two observed frequencies are due to Faraday rotation.

According to the BU-BLAZAR database, the EVPA in the core region of 0716+714 is fairly stable from the end of 2014 December until 2015 April, and changes are within 8°. Likely, there was a polarized feature with a reasonably stable EVPA that dominated the linearly polarized intensity in the core area, as we see in our SVLBI image for component C2 (Figure 2). Thus, it is unlikely that polarization properties significantly change over the five-day separation between our observations at 22 GHz and BU-BLAZAR observations at 43 GHz on 2014 December 29.

The 22 GHz RadioAstron image was convolved with the 43 GHz VLBA restoring beam size of 0.27 × 0.16 mas at 9°. We obtained a shift to the southwest of 0.018 mas to align the

---

[14] Partial release of the 18–22 cm MOJAVE observations: http://www.physics.ucc.ie/radiogroup/18-22cm_observations.html. The image is available at http://www.physics.purdue.edu/astro/MOJAVE/sourcepages/0716+714.shtml.

Table 2
Results of Gaussian Model Fitting of the 22 GHz SVLBI Data

Comp.	Flux Density (mJy)	Distance (μas)	PA (°)	Size (μas)	$T_{b,rf}$ (K)
Core	429 ± 56	4.8 ± 0.2	176 ± 6	<12 × 5	> 2.2 × 10^{13}
C1	212 ± 28	40.5 ± 0.5	153.7 ± 0.7	31.5 ± 0.4	(7.1 ± 0.9) × 10^{11}
C2	142 ± 19	58.0 ± 0.5	58.3 ± 0.3	19.1 ± 0.4	(1.29 ± 0.18) × 10^{12}
C3	146 ± 19	245 ± 3	51.9 ± 0.3	106.6 ± 0.8	(4.3 ± 0.6) × 10^{10}
C4	94 ± 13	358 ± 3	58.1 ± 0.2	107.5 ± 1.6	(2.70 ± 0.4) × 10^{10}
C5	12.0 ± 1.6	503 ± 6	37.6 ± 0.5	96 ± 7	(4.3 ± 0.8) × 10^{9}
C6	5.6 ± 0.8	613 ± 6	20.5 ± 0.5	39 ± 12	(1.1 ± 0.7) × 10^{9}
C7	5.8 ± 0.8	1168 ± 11	9.8 ± 1.3	455 ± 12	(9.2 ± 1.3) × 10^{7}
C8	3.8 ± 0.5	1878 ± 5	22.1 ± 0.2	211 ± 4	(2.8 ± 0.4) × 10^{8}

Note. The column identifiers correspond to: "Comp."—component label, "Flux"—flux density, "Distance"—distance from the map center, "PA"—position angle of the component from the map center, "Size"—component FWHM, and "$T_{b,rf}$"—rest frame brightness temperature (i.e., corrected for redshift and not corrected for Doppler boosting; see Equation (3)).

22 GHz image with respect to the 43 GHz one. No significant shift of the core position (coreshift) has been detected between these two frequencies, either by referencing the core position to the nearest optically thin component or using a 2D cross-correlation analysis (see e.g., Walker et al. 2000). The spectral index (defined as $S \propto \nu^{\alpha}$, where S is the flux density at an observing frequency ν) between the 22 GHz RadioAstron and 43 GHz VLBA images is shown in Figure 4, together with the resultant Faraday RM map.

The RM in the jet is consistent with zero value, whereas the core shows an RM of $-(5900 \pm 1100)$ rad m^{-2}. Lee et al. (2016) in their study measured RM between 22 and 43 GHz ranging between -9200 and 6300 rad m^{-2}, which is consistent with our estimates. The RM measured in the core can be reconciled with an external Faraday screen located near the jet. It is expected that adiabatic losses should result in the decaying particle density and magnetic field along the jet and in the Faraday screen around it, which can explain the higher RM observed in the core of 0716+714. The degree of linear polarization increases from a few percent in the core up to 50 percent at the position of component C4 (Figure 2). Together with the RM gradient along the jet, it may imply significant depolarization near the core region. The intrinsic EVPA, corrected for the Faraday rotation (Figure 4) is consistent with the dominance of the toroidal component of the ordered magnetic field in the blazar jet.

3.3. Timescale of Variability

Following Jorstad et al. (2017), the shortest variability timescale τ expected for component C2 can be calculated using light travel arguments as

$$\tau \sim \frac{25.3 R D_{L}}{\delta (1 + z)}, \quad (1)$$

where D_{L} is the luminosity distance given in Gpc, R is the FWHM of the circular Gaussian derived from the model fitting in mas, and τ is in years. Using the estimated component's size of $R = 19 \mu$as (see Table 2) and the largest observed Doppler factor of ~ 25 (Bach et al. 2005; Jorstad et al. 2017), we obtain $\tau \sim 8.6$ days for C2. Considering the resolution limit of $R < 5 \mu$as (Lobanov 2005), we obtain $\tau \leqslant 2.3$ days for the unresolved core. Assuming intrinsic origin of the IDV observed in 0716+714, these components explain the total and polarized

flux density variations observed in it on scales from a day to a week. Presence of a more compact component is required to describe the faster, hour-scale variability also reported in 0716+714 (e.g., Quirrenbach et al. 1989; Bach et al. 2006; Bhatta et al. 2015).

3.4. Jet Orientation and Flaring Activity in 0716+714

In order to study the evolution of the jet orientation and its potential relation with the jet emission we combine information about the position angle of the inner jet and the flaring activity in the source during the time period 2012–2017 (see Figure 5).

The PA changes are obtained from analysis of the 50 epochs made within the VLBA-BU-BLAZAR program at 43 GHz. To compare different epochs, we convolve all images with the same beam size of 0.23 × 0.16 mas at 0°, which corresponds to the average beam size over these epochs. To describe the jet PA we construct ridgelines for each epoch and calculate its direction in the inner 100 μas from the core. The ridgelines were obtained as the weighted average of the jet emission at a given radial distance from the core, following Pushkarev et al. (2017). The algorithm is based on azimuthal slicing of the source image, centered on the core. It searches for the weighted average along the slice, i.e., the point where the intensity integrated along the arc is equal on two sides, using pixels with S/N >3. The procedure repeats for each slice down the jet. The final ridgeline is constructed by fitting a cubic spline. The subtracted PAs are given in Figure 5.

The flaring activity was investigated using the measurements from the Metsähovi 13.7 m dish monitoring program at 37 GHz and the VLBA-BU-BLAZAR program at 43 GHz. The radio light curves at these frequencies in Figure 5 show two large flares at the beginning and mid 2013, followed by other minor outbursts. Our RadioAstron observations were taken in between some of these minor flares, when its flux density at 37 GHz reached ~ 1.4 Jy. This is thrice the flux density registered at the absolute minimum (~ 0.4 Jy, 2012 June), and a quarter of the absolute maximum (5.8 Jy, 2013 July) during 2012–2017.

Following Valtaoja et al. (1999) and Lähteenmäki et al. (1999), the flux density variations can be decomposed into individual flares, providing estimates of their physical parameters. In order to decompose the observed total flux density variations, we modeled the 37 GHz Metsähovi light curve with
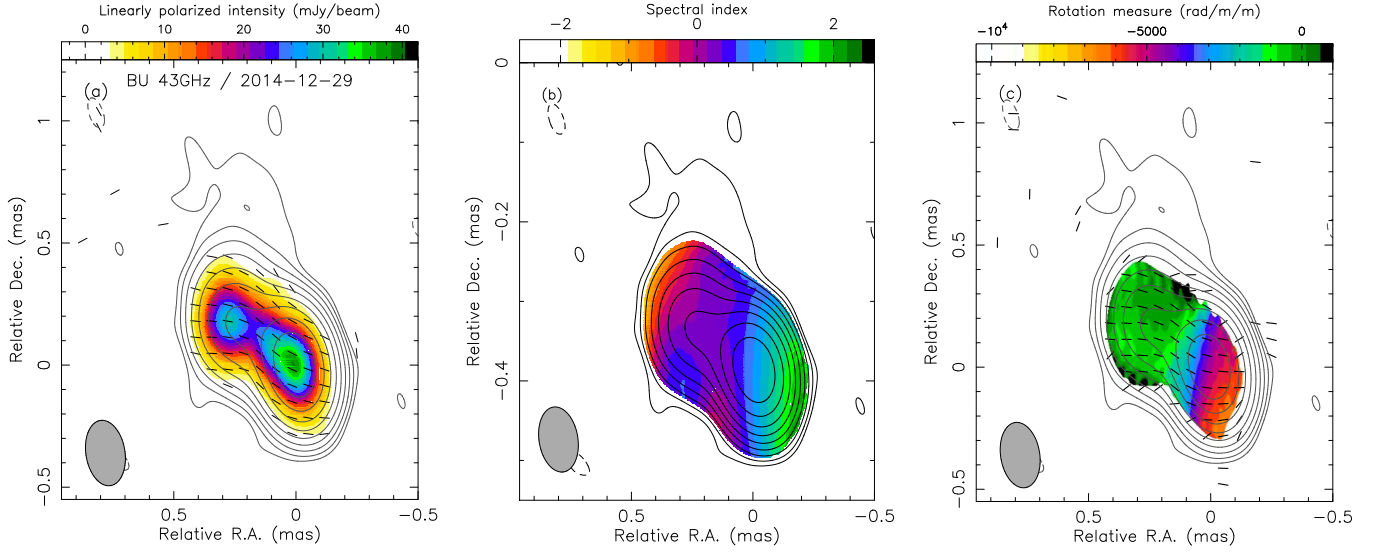
Figure 4. (a) VLBA-BU-BLAZAR image of 0716+714 at 43 GHz obtained at 2014 December 29. The total intensity contours are plotted at −2.3, 2.3, 4.6, 9.3, 18.6, 37.2, 74.3, 148.6, 297.3, 594.5, 1189.0 Jy/beam. Linearly polarized intensity is shown in colors starting at 2.1 mJy/beam, and bars indicate the EVPA. The synthesized beam FWHM is 0.27 × 0.16 mas at a position angle of 9°. (b) Spectral index image between the 22 GHz RadioAstron and 43 GHz VLBA-BU-BLAZAR total intensity images, convolved with the 43 GHz beam, and overlaid on Stokes *I* contours at 43 GHz. (c) Rotation measure map combining the images at 22 GHz and 43 GHz, and overlaid on Stokes *I* contours at 43 GHz. The colors indicates the rotation measure in rad m^{-2}, and the ticks indicate the Faraday-corrected EVPAs at 43 GHz.

a number of individual flares with the following profile

$$S(t) = \begin{cases} S_{\max} e^{(t-t_{\max})/\tau_{\mathrm{var}}}, & t < t_{\max}, \\ S_{\max} e^{(t_{\max}-t)/1.3\tau_{\mathrm{var}}}, & t > t_{\max}, \end{cases} \quad (2)$$

where $S_{\max}$ is the maximum amplitude of the flare, $t_{\max}$ is the epoch of the flare maximum, and τ_{var} is the flare-rise timescale. We identified and fit 27 individual flares, and provide the results of their decomposition in Figure 5 and in Table 3.

As can be seen from Figure 5, the jet experiences sudden changes in the PA in the middle of 2014, when its orientation changes from ∼20° to ∼70° and then returns back to ∼20° within a year. Lister et al. (2013) observed periodic variability of the jet PA in 0716+714 at larger scales and estimated a variability amplitude of ∼11° and a period of 10.9 yr for its variability.

We split the observing epochs into three groups, covering three different time ranges, and isolating the time period when the blazar had the most extreme eastward PA orientation. These ranges correspond to (a) 2012 January 27–2014 February 24, (b) 2014 May 3–2015 May 11, and (c) 2015 June 9–2017 April 16 (Figure 5) and are used to construct stacked images of the source presented in Figure 6. As can be seen, our space-VLBI observations probe the source in the middle of the most eastward orientation of the jet. From Figure 5, there is no indication for the correlation of variations between the total flux density and the jet PA at scales of 100 μas from the core. This suggests that the variability of the total flux density originates at smaller scales.

3.5. Variability, Brightness Temperature, and Doppler Boosting

We compute the brightness temperatures $T_{\mathrm{b,rf}}$ of the model-fitted VLBI components in the source rest frame as

(Kovalev et al. 2005)

$$T_{\mathrm{b,rf}} = 1.22 \times 10^{12} \frac{(1+z)S}{\nu^2 \theta_{\mathrm{maj}} \theta_{\mathrm{min}}} \ (\mathrm{K}), \quad (3)$$

where θ_{maj} and θ_{min} are the major and minor axes of the Gaussian component in mas, S is the flux density of the component in Jy, and the observing frequency, ν, is given in GHz. We can compare the brightness temperatures of the model-fitted components with the variability brightness temperatures calculated from the flare fits described above. The variability brightness temperature (in the source rest frame), $T_{\mathrm{b,var}}$, is given by

$$T_{\mathrm{b,var}} = 1.05 \times 10^8 \frac{D_{\mathrm{L}}^2 S}{(1+z)\nu^2 \tau_{\mathrm{var}}^2} \ (\mathrm{K}), \quad (4)$$

where luminosity distance D_{L} is given in Mpc and τ_{var} (yr) is the logarithmic variability timescale, defined as

$$\tau_{\mathrm{var}} = \frac{dt}{d \ln S}. \quad (5)$$

The variability brightness temperature is related to the variability Doppler factor δ_{var} and the intrinsic brightness temperature by

$$T_{\mathrm{b,var}} = \delta_{\mathrm{var}}^3 T_{\mathrm{b,int}}. \quad (6)$$

On the other hand, the rest frame $T_{\mathrm{b,rf}}$ and intrinsic $T_{\mathrm{b,int}}$ brightness temperatures in the VLBI core are connected through the Doppler boosting factor as

$$T_{\mathrm{b,rf}} = \delta \ T_{\mathrm{b,int}}. \quad (7)$$

Combining Equations (6) and (7), it is possible to estimate the Doppler factor and intrinsic brightness temperature. We use the results of the flare decomposition of the light curve and follow two different methods: (i) assume the value of intrinsic
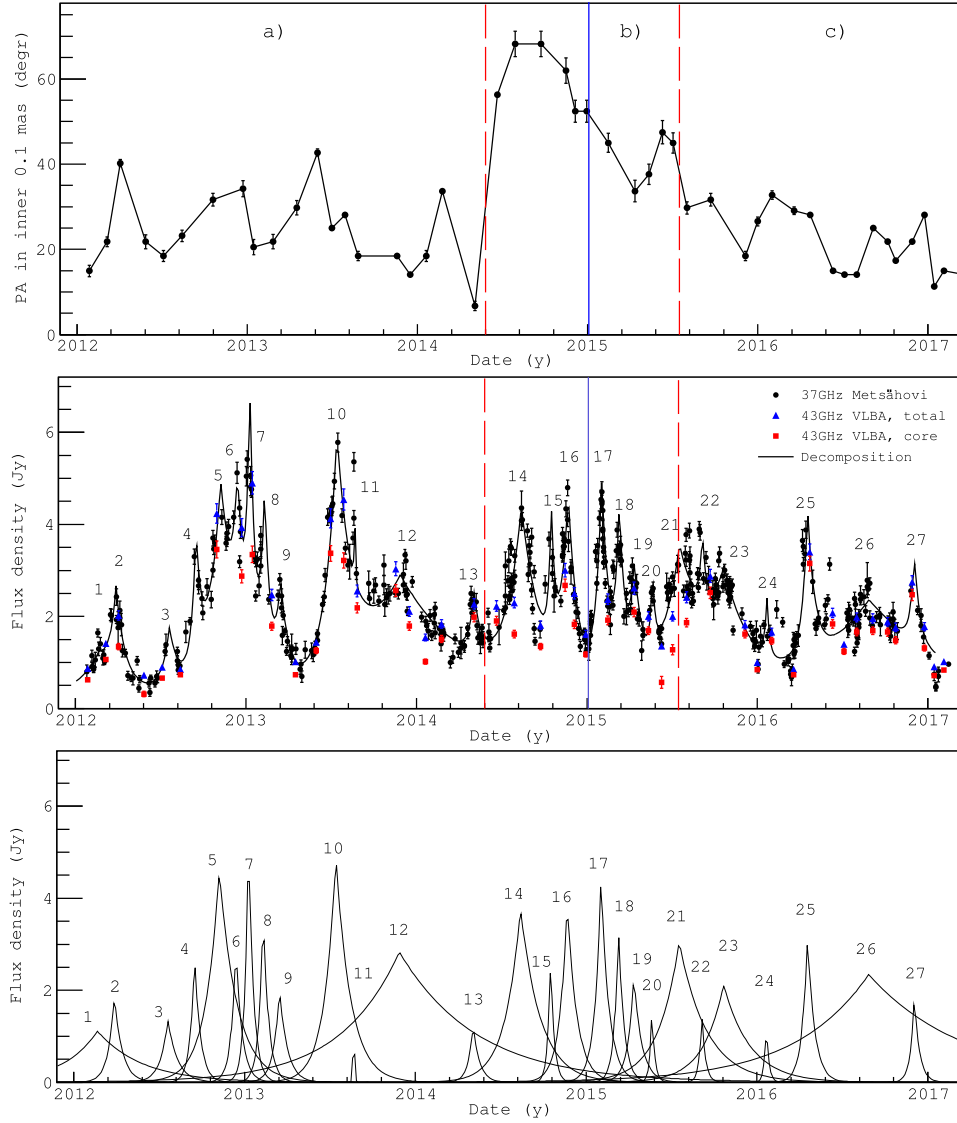
Figure 5. (Top) The jet PA in the inner 100 μas at 43 GHz. The vertical red dashed lines and letters mark three time ranges that were used to construct stack images, given in Figure 6. The vertical solid blue line indicates the epoch of RadioAstron observations. (Middle) 0716+714 total flux density at 37 GHz (black circles, Metsähovi), integrated flux density on the VLBA 43 GHz image (blue triangles), and core flux density at 43 GHz (red squares). The black solid line represents the results of the decomposition, which is a sum of individual exponential model flares shown in the bottom plot.

brightness temperature, and (ii) utilize both variability and VLBI data.

Method 1: for $T_{b,int}$ we assumed the equipartition value of 5×10^{10} K (Readhead 1994), as discussed in Lähteenmäki et al. (1999). Considering all model-fitted flares, it yields a range of Doppler factor values of $3 \leqslant \delta \leqslant 31$ (excluding outlier $\delta \sim 95$), with a median of ~18. The fastest flares provide better estimate of the Doppler factor, since they suffer less from the smearing with other flares and likely reach limiting brightness temperature. For the fastest model-fitted flares, δ is ~30 and is slightly higher than the maximum value of $\delta \sim 25$ that has been obtained in other studies of the source (e.g., Bach et al. 2005; Jorstad et al. 2017). This may imply that $T_{b,int}$ exceeds $T_{b,eq}$ during some flares.

Method 2: to calculate rest-frame brightness temperatures of the VLBI jet, we used observations of the blazar performed at 43 GHz with the VLBA. We selected the epochs that are observed close in time to the maxima of the decomposed flares (within the τ_{var}). We were able to identify eight flares that meet

the criterion. The respective *modelfit* parameters of the VLBI core and the estimated $T_{b,rf}$, calculated with Equation (7), are given in Table 3. The estimated values of the Doppler factor lie in the range $1 \lesssim \delta \lesssim 15$, and the intrinsic brightness temperature estimates are $(0.2–2) \times 10^{12}$ K (see Table 3).

3.6. RadioAstron 22 GHz Brightness Temperature: Breaking the Inverse-Compton Limit?

In case of inverse-Compton losses in incoherent synchrotron sources, it is expected that the intrinsic brightness temperature does not exceed the value of $T_{b,ic} \approx 10^{11.5}$ K (Kellermann & Pauliny-Toth 1969). Meanwhile, for the equipartition regime between the energy densities of the magnetic field and radiating particles, the value of $T_{b,eq} \sim 5 \times 10^{10}$ K has been obtained (Readhead 1994).

The results of model fitting of RadioAstron data yield brightness temperatures of 7×10^{11} K for C1, 1.3×10^{12} K for C2, and $T_b > 2.2 \times 10^{13}$ K for the core. The T_b computed for all the fitted components are given in Table 2.

Table 3
Results of Decomposition of the 37 GHz Light Curve into Individual Flares and Model Fitted Results for the Core Component at 43 GHz at Corresponding Epochs

Flare	S_{max} (Jy)	t_{max}[a] (yr)	τ_{var} (yr)	$\log_{10}(T_{b,var})$ (K)	δ_{var}	S_{core} (Jy)	BU Epoch (yr)	Size (μas)	$\log_{10}(T_{b,rf})$ (K)	$\log_{10}(T_{b,int})$ (K)	δ
1	1.11 ± 0.06	2012.14	0.203 ± 0.055	12.58 ± 0.09	4.2	⋯	⋯	⋯	⋯	⋯	⋯
2	1.88 ± 0.14	2012.24	0.036 ± 0.007	14.30 ± 0.16	15.9	⋯	⋯	⋯	⋯	⋯	⋯
3	1.35 ± 0.25	2012.55	0.045 ± 0.016	13.98 ± 0.52	12.4	⋯	⋯	⋯	⋯	⋯	⋯
4	2.78 ± 0.34	2012.71	0.026 ± 0.005	14.75 ± 0.21	22.5	⋯	⋯	⋯	⋯	⋯	⋯
5	4.60 ± 0.22	2012.85	0.081 ± 0.020	13.99 ± 0.17	12.5	3.46 ± 0.18	2012.83	47.1 ± 0.4	12.13 ± 0.02	11.20 ± 0.09	8.5 ± 0.2
6	2.91 ± 0.32	2012.95	0.028 ± 0.014	14.70 ± 0.44	21.6	2.87 ± 0.14[b]	2012.94	21.8 ± 0.9	12.72 ± 0.04	11.73 ± 0.35	9.8 ± 0.5
7	5.37 ± 0.27	2013.02	0.022 ± 0.003	15.18 ± 0.14	31.2	3.35 ± 0.18	2013.04	20.1 ± 1.3	12.86 ± 0.06	11.69 ± 0.12	14.5 ± 1.0
8	3.63 ± 0.50	2013.11	0.025 ± 0.006	14.91 ± 0.32	25.3	⋯	⋯	⋯	⋯	⋯	⋯
9	2.02 ± 0.14	2013.20	0.036 ± 0.004	14.35 ± 0.21	16.5	⋯	⋯	⋯	⋯	⋯	⋯
10	4.92 ± 0.12	2013.53	0.067 ± 0.003	14.18 ± 0.04	14.5	⋯	⋯	⋯	⋯	⋯	⋯
11	2.67 ± 0.26	2013.64	0.003 ± 0.001	16.63 ± 0.51	94.5	⋯	⋯	⋯	⋯	⋯	⋯
12	2.83 ± 0.04	2013.91	0.348 ± 0.017	12.52 ± 0.04	4.0	2.56 ± 0.13[c]	2013.87	34.2 ± 2.8	12.28 ± 0.08	12.16 ± 0.12	1.3 ± 0.1
13	1.25 ± 0.08	2014.34	0.029 ± 0.004	14.31 ± 0.10	16.0	1.99 ± 0.10	2014.34	30.6 ± 1.2	12.26 ± 0.04	11.24 ± 0.08	10.5 ± 0.5
14	3.78 ± 0.10	2014.62	0.090 ± 0.005	13.82 ± 0.05	10.9	⋯	⋯	⋯	⋯	⋯	⋯
15	2.77 ± 0.24	2014.79	0.016 ± 0.002	15.17 ± 0.23	31.0	⋯	⋯	⋯	⋯	⋯	⋯
16	3.91 ± 0.09	2014.89	0.044 ± 0.002	14.45 ± 0.04	17.8	⋯	⋯	⋯	⋯	⋯	⋯
17	4.38 ± 0.09	2015.09	0.037 ± 0.002	14.66 ± 0.04	20.9	⋯	⋯	⋯	⋯	⋯	⋯
18	3.35 ± 0.13	2015.19	0.025 ± 0.002	14.87 ± 0.08	24.6	⋯	⋯	⋯	⋯	⋯	⋯
19	2.28 ± 0.12	2015.28	0.036 ± 0.004	14.38 ± 0.09	16.9	2.09 ± 0.10	2015.28	16.54 ± 1.2	12.82 ± 0.07	12.04 ± 0.11	6.0 ± 0.5
20	1.62 ± 0.20	2015.38	0.013 ± 0.002	15.15 ± 0.51	30.5	⋯	⋯	⋯	⋯	⋯	⋯
21	3.04 ± 0.07	2015.54	0.124 ± 0.009	13.44 ± 0.06	8.2	⋯	⋯	⋯	⋯	⋯	⋯
22	1.48 ± 0.20	2015.68	0.016 ± 0.004	14.90 ± 0.23	25.2	⋯	⋯	⋯	⋯	⋯	⋯
23	2.12 ± 0.09	2015.80	0.121 ± 0.010	13.31 ± 0.04	7.4	⋯	⋯	⋯	⋯	⋯	⋯
24	1.30 ± 0.35	2016.05	0.012 ± 0.004	15.11 ± 0.12	29.5	⋯	⋯	⋯	⋯	⋯	⋯
25	3.16 ± 0.16	2016.30	0.032 ± 0.002	14.63 ± 0.06	20.5	3.15 ± 0.16	2016.31	24.1 ± 0.5	12.67 ± 0.03	11.69 ± 0.05	9.5 ± 0.3
26	2.34 ± 0.03	2016.65	0.435 ± 0.029	12.24 ± 0.05	3.3	⋯	⋯	⋯	⋯	⋯	⋯
27	1.83 ± 0.28	2016.92	0.024 ± 0.005	14.67 ± 0.15	21.0	2.47 ± 0.12	2016.91	19.5 ± 0.7	12.75 ± 0.04	11.79 ± 0.09	9.1 ± 0.4

Note. Decomposed flares are shown in Figure 5. See Section 3.4 for details.
[a] Typical error is of the order of a day.
[b] Fitted model is not reliable.
[c] The core is modeled by an elliptical Gaussian component.

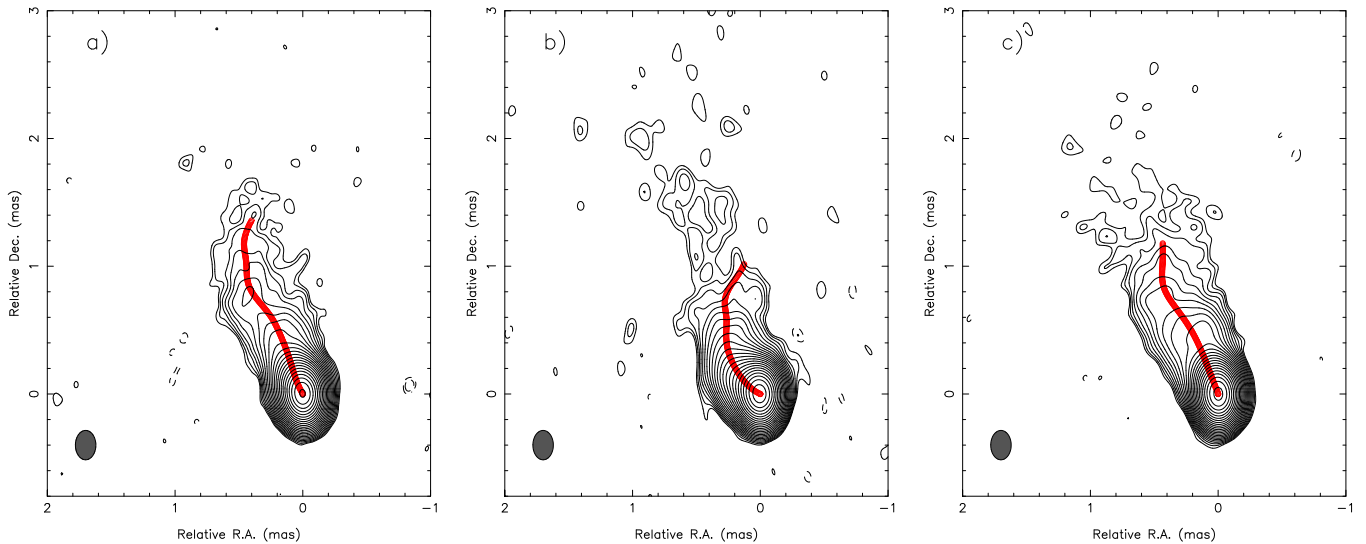(This table is available in machine-readable form.)

Figure 6. Stacked images of 0716+714 at 43 GHz and evolution of the jet shape and ridgeline with time. (a) 19 epochs from 2012 January 27 to 2014 February 24. (b) 10 epochs from 2014 May 3 to 2015 May 11. (c) 21 epochs between 2015 June 9 and 2017 April 16. The ridgeline is given as a number of red circles. The naturally weighted beam is 0.23x0.16 mas at 0 deg and is shown at the left bottom corner.

Comparison of the Gaussian *modelfit* results for components C1 and C2 shows that the size of C1 appears to be larger than the size of C2 and $T_{b,C1} < T_{b,C2}$. From the adiabatic expansion and conical jet models (See Kadler et al. 2004 and references therein), the linear dependence of T_b and size of the components with distance along the jet are expected. There a number of possibilities that may account for this. First of all, the linear behavior requires several conditions: no changes in physical conditions (e.g., absorption) along the strait and continuous jet, constant or slightly varying Doppler factor and jet viewing angle. In Sections 3.4 and 3.5 we show that some of these parameters vary with time. Changes in the collimation profile of the jet from being parabolic to being conical (Asada & Nakamura 2012; Kovalev et al. 2019) will have an impact on this relation. Blending effects near the core region may be significant, affecting the *modelfit* results for the size and flux density of component C1. Different position angles, at which components C1 and C2 were ejected into the jet (Lister et al. 2013), and subsequent projection effects, will also alter the results.

The brightness temperature in the jet can differ from the estimate, as shown by a representation of the structure by a series of Gaussian components. In this case, the minimum brightness temperature $T_{b,min}$ that can be obtained from our data can be directly estimated from the visibility amplitudes, under the condition that structural details sampled by the given visibility are resolved (see Lobanov 2015 for further details). Considering the visibility amplitude on the largest projected baseline between RadioAstron and Green Bank (of ∼5.2 Gλ on average), the observed brightness temperature of the most compact structure must exceed 9×10^{12} K. This agrees with the T_b obtained from the Gaussian model fit for the most compact structure in 0716+714 jet, the core.

According to Equation (7) and considering the maximum Doppler factor of $\delta \approx 25$, reported by the ground-based kinematic studies of 0716+714 (e.g., Bach et al. 2005; Jorstad et al. 2017) and consistent with our estimates in Section 3.5, the RadioAstron observations yield $T_{b,int} \geqslant 9 \times 10^{11}$ in the rest frame of the flow. It also agrees well with our estimate of $T_{b,int} = (0.1–2.0) \times 10^{12}$ K above. These estimates imply a

departure of physical conditions in the inner jet from the equipartition between magnetic field and relativistic particle energy densities, and are also larger than the inverse-Compton brightness limit.

Kovalev et al. (2016) suggested that some internal phenomenon may be responsible for producing extremely high brightness temperature, over the Compton catastrophe limit. The findings of Bruni et al. (2017) show that the states when $T_{b,int}$ breaks the abovementioned limits may be connected with the activity of the sources. Indeed, Jorstad et al. (2017) in observed a few cases when the $T_{b,int}$ of the cores exceeds $T_{b,eq}$ by a factor of 10 and associated all of them with strong multiwavelength activity of the sources.

Three weeks after our RadioAstron observations the MAGIC Collaboration et al. (2018) detected unprecedented outbursts in 0716+714 at very high energies (VHE), peaking on January 25 and February 14. The MAGIC study also reports the ejection of a new jet component (K14b, in their notation) that passed through the VLBI core about 55 days before the first VHE flare and moved out with a proper motion of (0.51 ± 0.09) mas yr^{-1}. MAGIC Collaboration et al. (2018) interpreted the VHE flares as being produced by the interaction of this moving component with the stationary feature A1 reported by Rani et al. (2015) and Jorstad et al. (2017), which was considered to be a recollimation shock. Using the measured proper motion of K14b and back-extrapolating its position to the epoch of our RadioAstron observations, we localized it at a distance of 63 ± 42 μas from the core. It applies that either component C1 or C2 may be corresponding to the component K14b associated with the VHE and multiband flaring activity observed in 0716 +714 at the beginning of 2015.

3.7. Doppler Factor Variability?

In the case of a continuous, extended jet, the apparent flux will be enhanced by at least a factor of δ^2 relative to that in the AGN rest frame (Lind & Blandford 1985). A recent VLBI study at 86 GHz ($\lambda = 3$ mm, Nair et al. 2019) reports significant flux density variations in 0716+714. From the data taken at two different epochs, 2011 May 5 and 2011 October 9

(their Figure 6), the following can be seen. The intensity of the extended structure in the jet at the first epoch is about 600 mJy/beam. Meanwhile, five months later this structure is not visible down to a level of $\sim$20 mJy/beam. If the variability is solely due to changes in the amount of Doppler boosting, this thirtyfold decrease in flux requires about a five times change in the Doppler factor. Meanwhile, flux variations obtained at 43 GHz (Figure 5) are less pronounced and imply a change in δ bof a factor of three. Our results of the light-curve decomposition indeed indicate (Section 3.4) Doppler factor variability.

If we assume a scenario where rapid variations in Doppler factor are partially due to changes in the jet viewing angle and may be associated with the fast variability observed in the source, we can estimate the respective changes of the jet viewing angle. For the maximum observed apparent velocity $\beta_{\rm app} \approx 25c$ (Jorstad et al. 2017), the required minimum Lorentz factor $\Gamma_{\rm min} = (1+\beta_{\rm app}^2)^{1/2} \approx 25$, yields the velocity of the jet components in units of the speed of light $\beta \approx 0.9992$. Using $\beta \cos\theta = 1 - (\delta\Gamma)^{-1}$, the Doppler factor variations in a range of $\delta \sim 5$ to $\delta \sim 15$ can be explained by the change in the jet orientation from $\theta \sim 7^\circ$ to $\theta \sim 4^\circ$.

4. Summary

We present space-VLBI observations of the blazar 0716+714 made with the RadioAstron mission at 22 GHz. The observations were performed as part of the AGN Polarization KSP on 2015 January 3–4. The source has been detected on the space–ground baselines up to 5.6 ED (70 833 km) in total and linearly polarized intensity. We constructed full-polarimetric images of 0716+714 with a restoring beam of 57 × 24 μas. At this resolution, we find the complex and significantly bent structure of the central 100 μas of the jet, which can be represented by two Gaussian components of 32 μas (C1) and 19 μas (C2) in size and an unresolved core of <12 × 5 μas in extent. The jet initially extends toward the southeast at a position angle of 153°.1 up to $\sim$41 μas (C1), followed by a sharp bend of about 95° toward the northeast at a distance $\sim$58 μas from the core (C2). Complementary analysis of the VLBA data at 43 GHz taken in 2012–2017 shows that our RadioAstron experiment was made close to the time when the blazar jet had the most eastward orientation during these five years of observations. We conclude, that the inner jet of 0716+714 appears bent, as it is observed at a viewing angle that is smaller than the opening angle of the conical outflow.

From a comparison of our RadioAstron results with the large-scale radio image of 0716+714, we see a $\sim$210° offset between orientations of the component C1 and the arcsec-scale structure of the jet relative to the core. Due to projection effects, this apparent PA offset may correspond to an intrinsic bend of the jet of about $\sim$10°. The mechanism capable of producing this curved structure of the blazar remains open.

The polarization image of 0716+714 is characterized by a fairly strong 15% linearly polarized component, located $\sim$58 μas downstream from the core, which is represented by the model-fitted component of 19 μas in size. This jet component may be responsible for the intrinsic variability of the blazar total and polarized intensities timescales of about a week, while the unresolved core of the jet can be responsible for variability on timescales down to about two days.

From the joint analysis of our observations together with VLBA data at 43 GHz, we estimate RM of $-(5900 \pm 1100)\,{\rm rad\,m^{-2}}$ in the core. We do not detect significant Faraday rotation in the jet. We conclude that the external Faraday screen in close vicinity to the jet is the most promising explanation for the observed RM, and that the blazar jet has a well ordered magnetic field with a dominant toroidal component.

The intrinsic brightness temperature of the jet core is found to be $T_{\rm b,int} > 9 \times 10^{11}$ K when assuming the Doppler factor of $\delta \sim 25$. This value exceeds the equipartition and inverse-Compton limits by factors of 18 and 3, respectively. From the decomposition of the 37 GHz light curve into individual flares and ground-based VLBA observations, we estimate the Doppler factor values to lie in the range $1 \lesssim \delta \lesssim 15$, while intrinsic brightness temperature is found to vary between 2×10^{11} K and 2×10^{12} K. We suggest that variations of δ and $T_{\rm b,int}$ are due to changes in the jet viewing angle.

Facilities: RadioAstron Space Radio Telescope (Spektr-R), VLBA, Green Bank 100 m radio telescope, Sheshan 25 m radio telescope (Shangai), EVN, Effelsberg 100 m radio telescope, Noto 32 m radio telescope.

Software: AIPS (Greisen 2003), Difmap (Pearson et al. 1994), ROOT framework (Antcheva et al. 2009).

ORCID iDs

E. V. Kravchenko ⬤ https://orcid.org/0000-0003-4540-4095
J. L. Gómez ⬤ https://orcid.org/0000-0003-4190-7613
Y. Y. Kovalev ⬤ https://orcid.org/0000-0001-9303-3263
T. Savolainen ⬤ https://orcid.org/0000-0001-6214-1085
G. Bruni ⬤ https://orcid.org/0000-0002-5182-6289
J. M. Anderson ⬤ https://orcid.org/0000-0002-5989-8498
S. G. Jorstad ⬤ https://orcid.org/0000-0001-6158-1708
A. P. Marscher ⬤ https://orcid.org/0000-0001-7396-3332
M. Tornikoski ⬤ https://orcid.org/0000-0003-1249-6026
M. M. Lisakov ⬤ https://orcid.org/0000-0001-6088-3819

References

Antcheva, I., Ballintijn, M., Bellenot, B., et al. 2009, CoPhC, 180, 2499
Asada, K., & Nakamura, M. 2012, ApJL, 745, L28
Bach, U., Krichbaum, T. P., Kraus, A., Witzel, A., & Zensus, J. A. 2006, A&A, 452, 83
Bach, U., Krichbaum, T. P., Ros, E., et al. 2005, A&A, 433, 815
Bennett, C. L., Larson, D., Weiland, J. L., & Hinshaw, G. 2014, ApJ, 794, 135
Bhatta, G., Goyal, A., Ostrowski, M., et al. 2015, ApJL, 809, L27
Bruni, G., Anderson, J., Alef, W., et al. 2016, Galax, 4, 55
Bruni, G., Gómez, J. L., Casadio, C., et al. 2017, A&A, 604, A111
Danforth, C. W., Nalewajko, K., France, K., & Keeney, B. A. 2013, ApJ, 764, 57
Event Horizon Telescope Collaboration, Akiyama, K., Alberdi, A., et al. 2019a, ApJL, 875, L4
Event Horizon Telescope Collaboration, Akiyama, K., Alberdi, A., et al. 2019b, ApJL, 875, L2
Fuhrmann, L., Krichbaum, T. P., Witzel, A., et al. 2008, A&A, 490, 1019
Gabuzda, D. C., Kochenov, P. Y., Cawthorne, T. V., & Kollgaard, R. I. 2000, MNRAS, 313, 627
Gómez, J. L., Lobanov, A. P., Bruni, G., et al. 2016, ApJ, 817, 96
Greisen, E. W. 2003, in Information Handling in Astronomy—Historical Vistas, ed. A. Heck (Dordrecht: Kluwer), 109
Gupta, A. C., Krichbaum, T. P., Wiita, P. J., et al. 2012, MNRAS, 425, 1357
Hovatta, T., Valtaoja, E., Tornikoski, M., & Lähteenmäki, A. 2009, A&A, 494, 527
Hu, S. M., Chen, X., Guo, D. F., Jiang, Y. G., & Li, K. 2014, MNRAS, 443, 2940
Jennison, R. C. 1958, MNRAS, 118, 276
Jorstad, S. G., Marscher, A. P., Morozova, D. A., et al. 2017, ApJ, 846, 98
Kadler, M., Ros, E., Lobanov, A. P., Falcke, H., & Zensus, J. A. 2004, A&A, 426, 481
Kardashev, N. S., Alakoz, A. V., Andrianov, A. S., et al. 2017, SoSyR, 51, 535
Kardashev, N. S., Khartov, V. V., Abramov, V. V., et al. 2013, ARep, 57, 153

Kellermann, K. I., & Pauliny-Toth, I. I. K. 1969, ApJL, 155, L71
Kovalev, Y. Y., Kardashev, N. S., Kellermann, K. I., et al. 2016, ApJL, 820, L9
Kovalev, Y. Y., Kellermann, K. I., Lister, M. L., et al. 2005, AJ, 130, 2473
Kovalev, Y. Y., Pushkarev, A. B., Nokhrina, E. E., et al. 2019, arXiv:1907.01485
Kuehr, H., Witzel, A., Pauliny-Toth, I. I. K., & Nauber, U. 1981, A&AS, 45, 367
Lähteenmäki, A., Valtaoja, E., & Wiik, K. 1999, ApJ, 511, 112
Lee, J. W., Lee, S.-S., Kang, S., Byun, D.-Y., & Kim, S. S. 2016, A&A, 592, L10
Liao, N. H., Bai, J. M., Liu, H. T., et al. 2014, ApJ, 783, 83
Lind, K. R., & Blandford, R. D. 1985, ApJ, 295, 358
Lipunov, V., Kornilov, V., Gorbovskoy, E., et al. 2010, AdAst, 2010, 349171
Lister, M. L., Aller, M. F., Aller, H. D., et al. 2013, AJ, 146, 120
Lister, M. L., Aller, M. F., Aller, H. D., et al. 2018, ApJS, 234, 12
Lister, M. L., Homan, D. C., Hovatta, T., et al. 2019, ApJ, 874, 43
Liu, X., Song, H.-G., Marchili, N., et al. 2012, A&A, 543, A78
Lobanov, A. 2015, A&A, 574, A84
Lobanov, A. P. 2005, arXiv:astro-ph/0503225
Lobanov, A. P., Gómez, J. L., Bruni, G., et al. 2015, A&A, 583, A100
MAGIC Collaboration, Ahnen, M. L., Ansoldi, S., et al. 2018, A&A, 619, A45
Martí-Vidal, I., Pérez-Torres, M. A., & Lobanov, A. P. 2012, A&A, 541, A135
Nair, D. G., Lobanov, A. P., Krichbaum, T. P., et al. 2019, A&A, 622, A92
Nilsson, K., Pursimo, T., Sillanpää, A., Takalo, L. O., & Lindfors, E. 2008, A&A, 487, L29
Ostorero, L., Wagner, S. J., Gracia, J., et al. 2006, A&A, 451, 797
Pashchenko, I. N., Kovalev, Y. Y., & Voitsik, P. A. 2015, CosRe, 53, 199
Pearson, T. J., Shepherd, M. C., Taylor, G. B., & Myers, S. T. 1994, BAAS, 26, 1318
Planck Collaboration, Ade, P. A. R., Aghanim, N., et al. 2016, A&A, 594, A13
Pushkarev, A. B., Kovalev, Y. Y., Lister, M. L., & Savolainen, T. 2017, MNRAS, 468, 4992
Quirrenbach, A., Witzel, A., Krichbaum, T., Hummel, C. A., & Alberdi, A. 1989, Natur, 337, 442
Rani, B., Gupta, A. C., Joshi, U. C., Ganesh, S., & Wiita, P. J. 2010, ApJL, 719, L153
Rani, B., Krichbaum, T. P., Marscher, A. P., et al. 2015, A&A, 578, A123
Rastorgueva, E. A., Wiik, K., Savolainen, T., et al. 2009, A&A, 494, L5
Readhead, A. C. S. 1994, ApJ, 426, 51
Readhead, A. C. S., Nakajima, T. S., Pearson, T. J., et al. 1988, AJ, 95, 1278
Rickett, B. J., Coles, W. A., & Bourgois, G. 1984, A&A, 134, 390
Rogers, A. E. E., Hinteregger, H. F., Whitney, A. R., et al. 1974, ApJ, 193, 293
Savolainen, T., Wiik, K., Valtaoja, E., et al. 2006, ApJ, 647, 172
Shepherd, M. C. 1997, in ASP Conf. Ser. 125, Astronomical Data Analysis Software and Systems VI, ed. G. Hunt & H. Payne (San Francisco, CA: ASP), 77
Shepherd, M. C., Pearson, T. J., & Taylor, G. B. 1994, BAAS, 26, 987
Teraesranta, H., Tornikoski, M., Mujunen, A., et al. 1998, A&AS, 132, 305
Valtaoja, E., Lähteenmäki, A., Teräsranta, H., & Lainela, M. 1999, ApJS, 120, 95
Wagner, S., Sanchez-Pons, F., Quirrenbach, A., & Witzel, A. 1990, A&A, 235, L1
Wagner, S. J., & Witzel, A. 1995, ARA&A, 33, 163
Wagner, S. J., Witzel, A., Heidt, J., et al. 1996, AJ, 111, 2187
Walker, R. C., Dhawan, V., Romney, J. D., Kellermann, K. I., & Vermeulen, R. C. 2000, ApJ, 530, 233